Supporting Information for

Large Pore-Sized Organosilica Nanoparticles with Controlled Release of Glucose Oxidase for Tumor-Specific Cascaded Catalytic Therapy

Xiaobing Zhang,[†ab] Yuhang Huang,[†c] Wennan Li,[†c] Shuping Qu,[†b] YunHou,[c] Hongyu Pan,[b] Qiang Fang,[b] Dong Wu,*[b],Chao Zhang,*[a] Wenpei Fan*[cd] and Chong Zhang*[a]

[a] Department of General Surgery, The First Affiliated Hospital of Anhui Medical University, Hefei 230022, China.

[b] Department of Hepatic Surgery, Third Affiliated Hospital of Second Military Medical University, Shanghai 200082, China.

[c] State Key Laboratory of Natural Medicines and Jiangsu Key Laboratory of Drug Discovery for Metabolic Diseases, Center of Advanced Pharmaceuticals and Biomaterials, China Pharmaceutical University, Nanjing 211198, China.

[d] State Key Laboratory of Neurology and Oncology Drug Development, Nanjing 210042, China.

* Correspondence: wudong1005@sina.com (Dong Wu); 13965053990@163.com (Chao Zhang); wenpei.fan@cpu.edu.cn (Wenpei Fan); chongzhang93@126.com (Chong Zhang).

† These authors contributed equally.

Supplementary figures

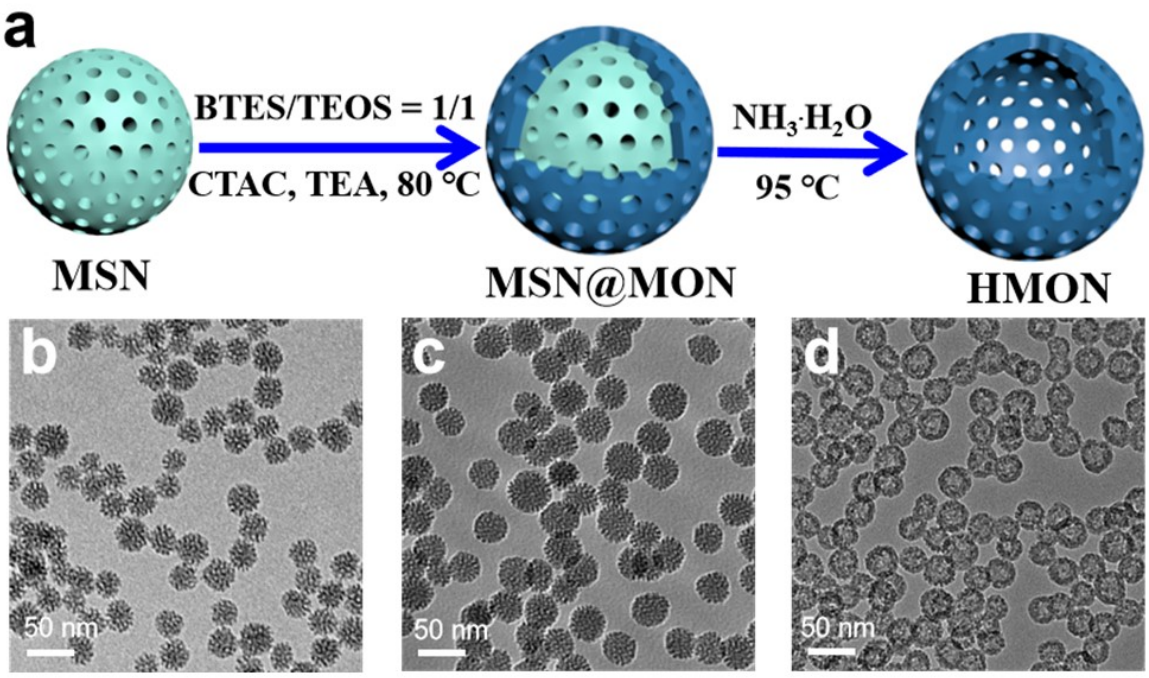

Figure S1. (a) Schematic representation for the synthesis of HMON by using the hybrid precursors with a BTES/TEOS ratio of 1:1. (b-d) TEM images of (b) MSN, (c) MSN@MON, and (d) HMON.

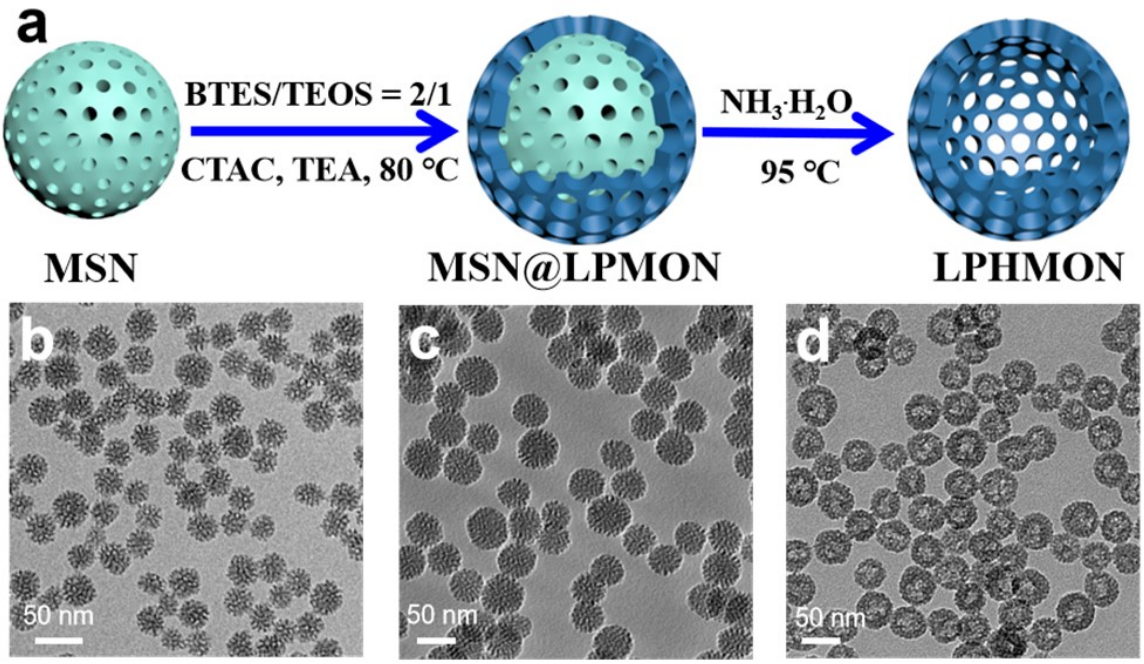

Figure S2. (a) Schematic representation for the synthesis of LPHMON by using the hybrid precursors with a BTES/TEOS ratio of 2:1. (b-d) TEM images of (b) MSN, (c) MSN@LPMON, and (d) LPHMON.

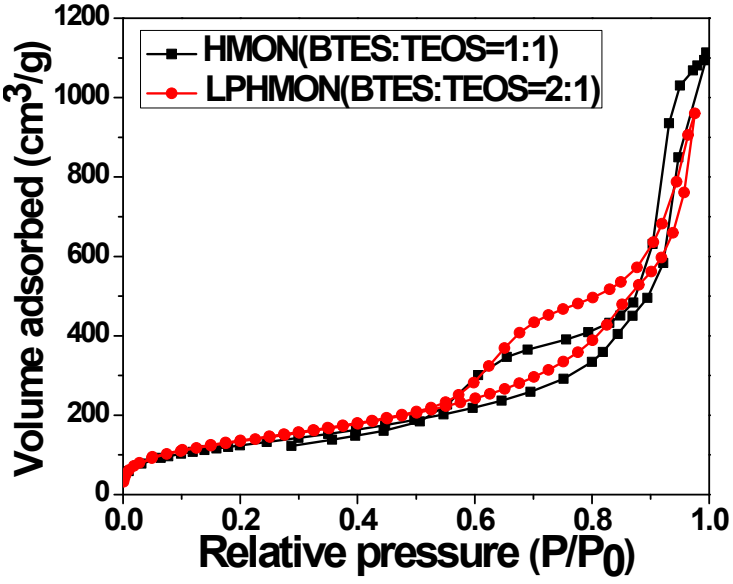

Figure S3. N_2 adsorption-desorption isotherms of HMON and LPHMON synthesized by using the hybrid precursors with BTES/TEOS ratios of 1:1 and 2:1, respectively. The BET surface areas of HMON and LPHMON are 430.47 m^2/g and 493.02 m^2/g, respectively.

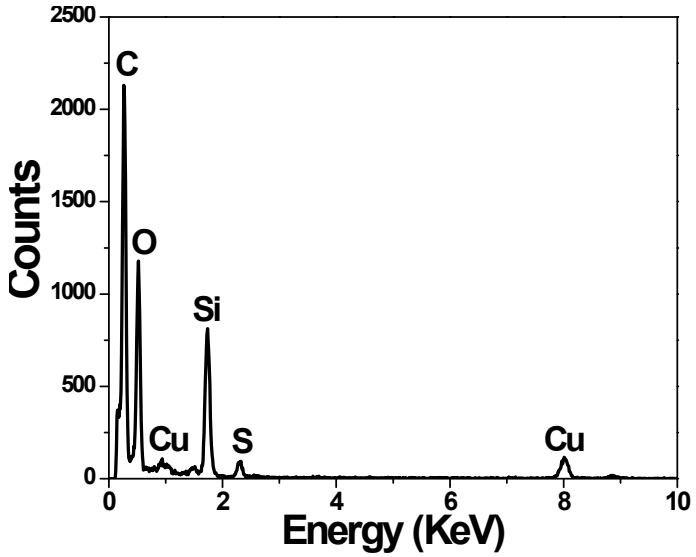

Figure S4. Energy-dispersive X-ray spectroscopy (EDS) spectrum of LPHMON-TC. All the major elements (Si, O, C, S, Cu) are shown in this spectrum. The S signal indicates the framework hybridization of LPHMON with thioether moieties, and the Cu signal indicates the surface modification of LPHMON with TA-Cu complex.

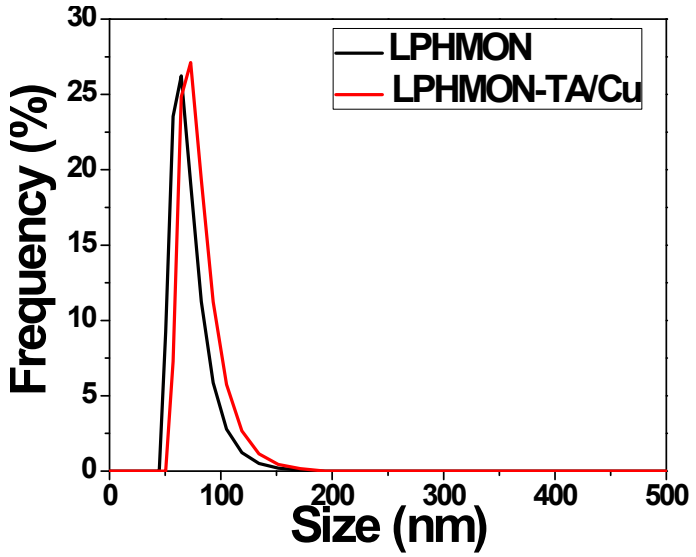

Figure S5. Dynamic light scattering (DLS) size measurement of (a) LPHMON and (b) LPHMON-TC in ultrapure water. The average hydrolyzed particle sizes of LPHMON and LPHMON-TC are 67.8 nm and 73.2 nm with polydispersity index (PDI) values of 0.248 and 0.158, respectively.

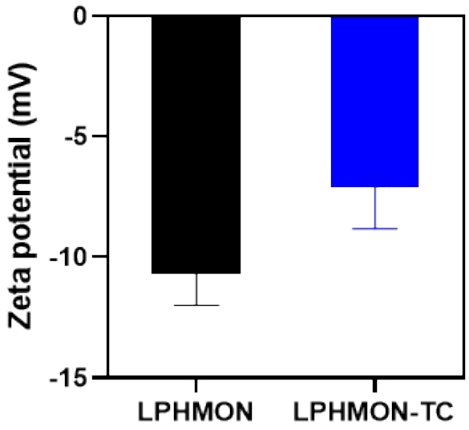

Figure S6. Zeta potentials of LPHMON and LPHMON-TC. n = 3, mean ± s.d.

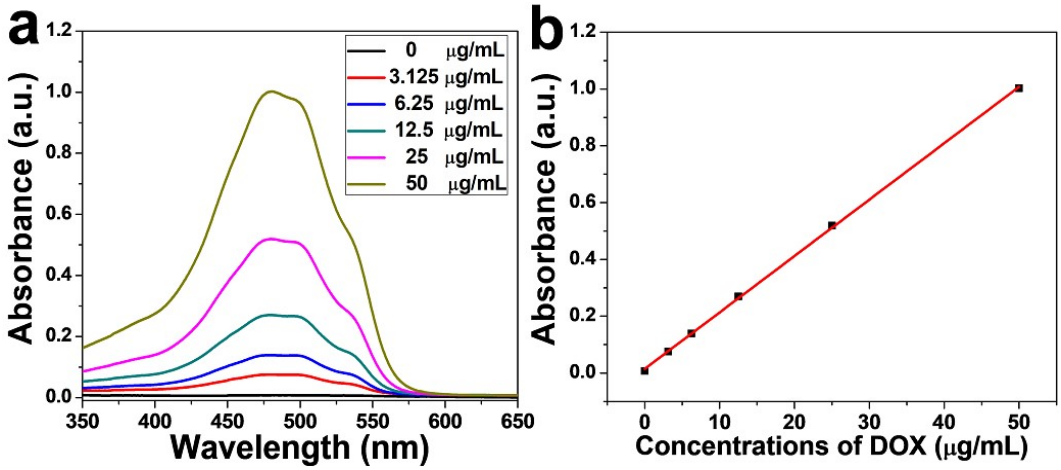

Figure S7. (a) UV/Vis absorption spectra of DOX with different concentrations (0, 3.125, 6.25, 12.5, 25, 50 μg/mL). (b) The standard curve showing the linear relation between the absorbance of DOX at λ = 480 nm and its concentration.

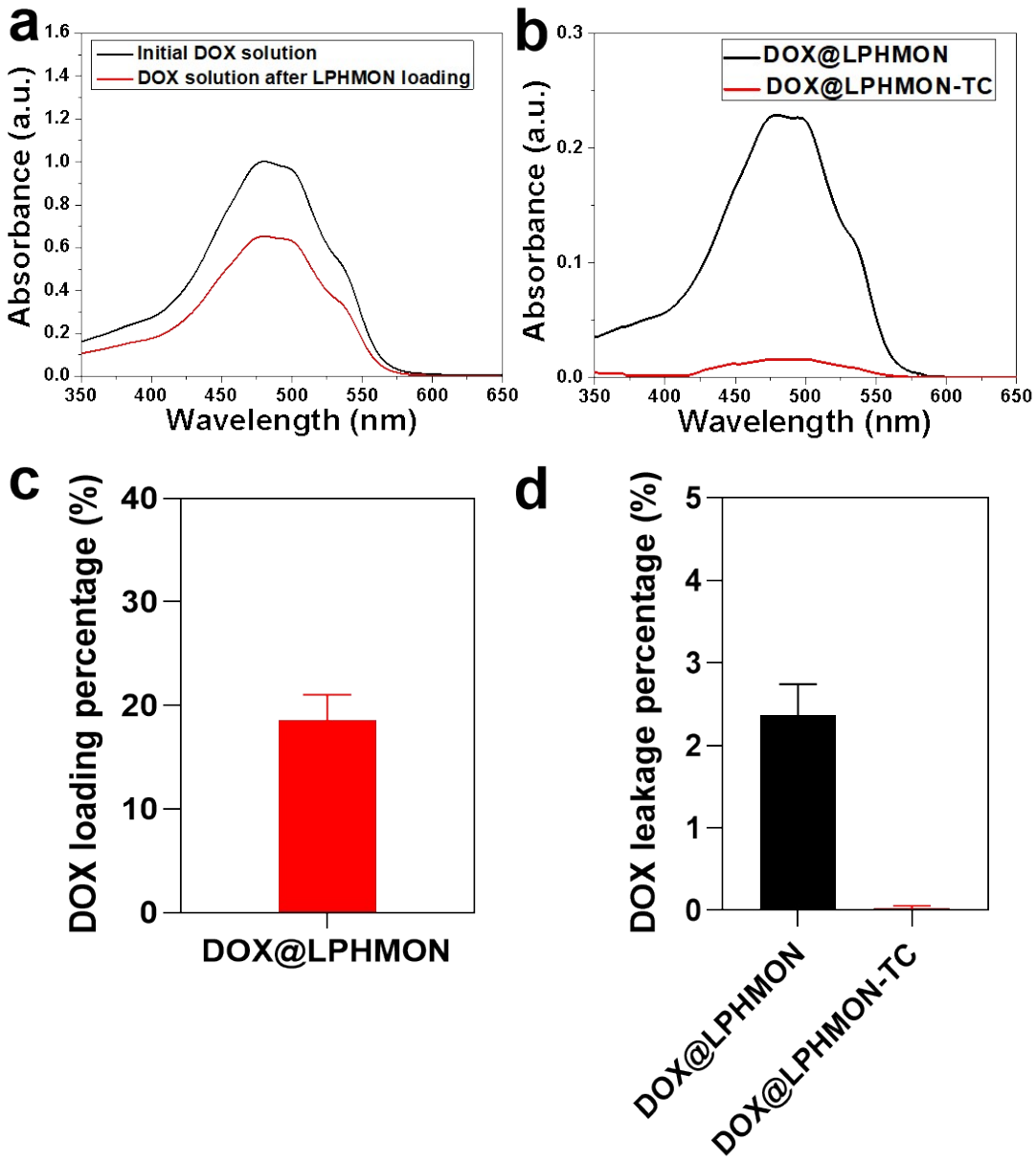

Figure S8. (a) UV/Vis absorption spectra of DOX solution before and after loading in LPHMON. The DOX loading capacity of LPHMON is about 18 wt.%. (b) UV/Vis absorption spectra of DOX supernatant of DOX@LPHMON and DOX@LPHMON-TC in water after centrifugation. (c) Loading rate of DOX and (d) release rate of DOX before and after TA-Cu coating. About 2.4% DOX was leaked from DOX@LPHMON after centrifugation, while little (only 0.03%) DOX was leaked, which indicated the advantage of the surface-decorated TA-Cu shell in preventing the DOX leakage from LPHMON.

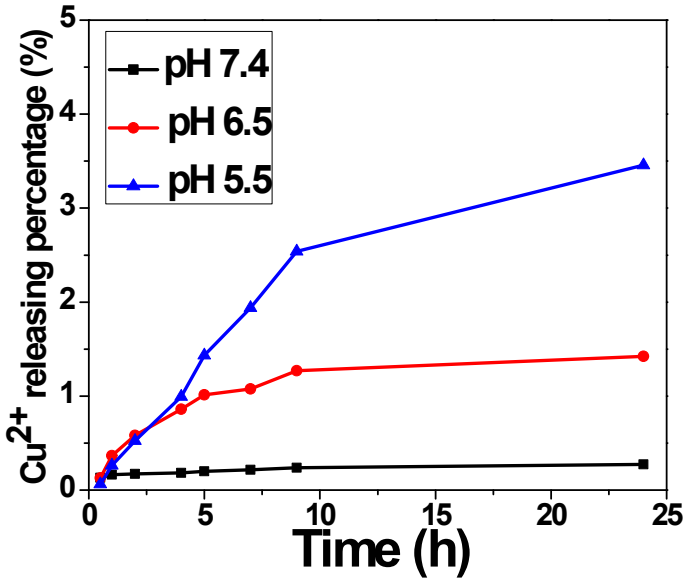

Figure S9. Release profiles of Cu^{2+} (measured by ICP-OES) from LPHMON-TC during 24 h of incubation in PBS at different pH (7.4, 6.5, 5.5). The specific Cu^{2+} release at pH 6.5 and 5.5 indicates the decomposition of TA-Cu complex in the acidic solution.

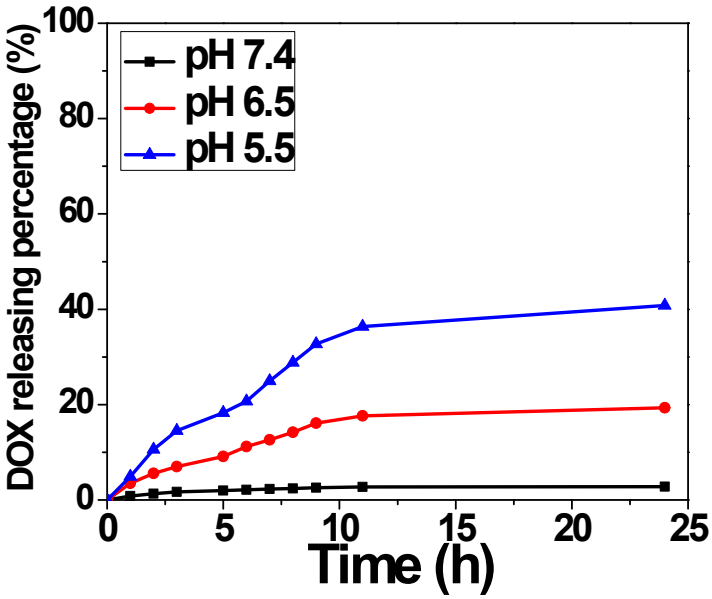

Figure S10. Release profiles of DOX from DOX-loaded LPHMON-TC during 24 h of incubation in PBS at different pH (7.4, 6.5, 5.5). The unreleased DOX was attributed to the incomplete disassociation of TA-Cu coating plus the electric attraction between positive DOX molecules and negative silica shell.

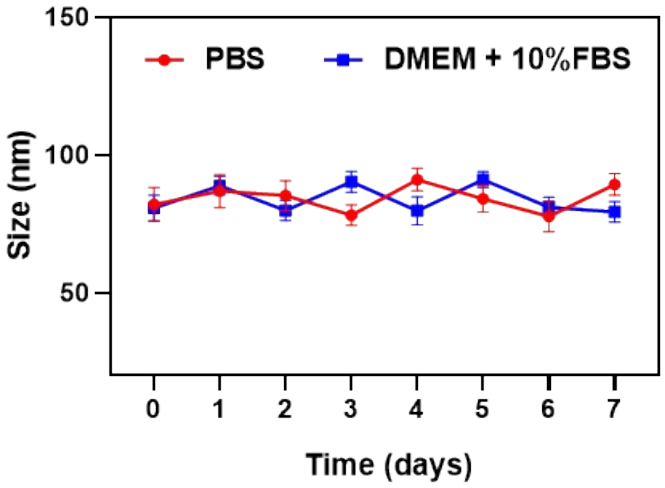

Figure S11. Size changes of LPHMON-GTC in PBS and DMEM medium containing 10% FBS for seven days. n = 3, mean ± s.d.

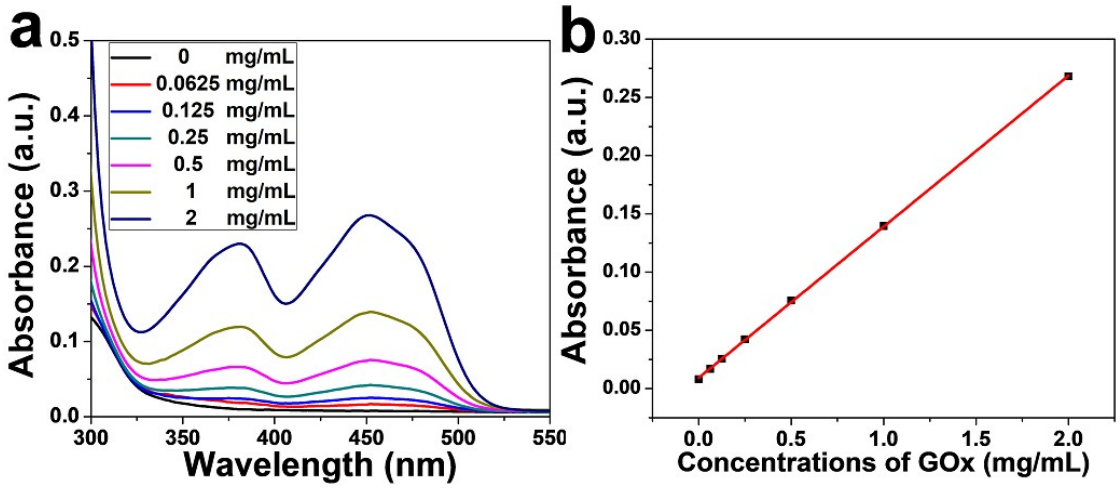

Figure S12. (a) UV/Vis absorption spectra of GOx with different concentrations (0, 0.0625, 0.125, 0.25, 0.5, 1, 2 mg/mL). (b) The standard curve showing the linear relation between the absorbance of GOx at λ = 452 nm and its concentration.

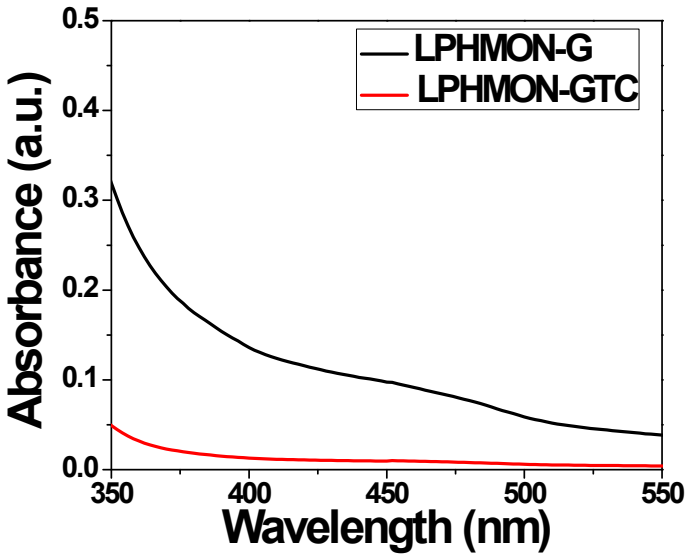

Figure S13. UV/Vis absorption spectra of GOx supernatant of LPHMON-G and LPHMON-GTC in water after centrifugation. About 40.1% GOx was leaked from LPHMON-G after centrifugation, while only 0.3% GOx was leaked, which indicated the advantage of the surface-decorated TA-Cu shell in preventing the GOx leakage from LPHMON.

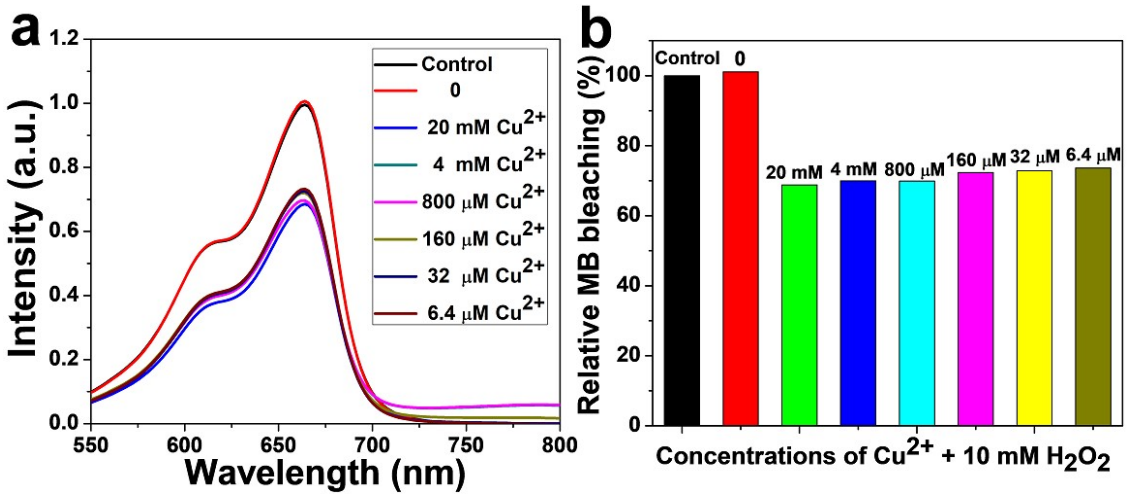

Figure S14. Evaluation of •OH yield (determined by the decay of MB absorption at λ = 664 nm) arising from the Fenton-like reaction between 10 mM H_2O_2 and varied concentrations of Cu^{2+}. (a) UV/Vis absorption spectra of methylene blue (MB) in the mixed solution of 10 mM H_2O_2 and different concentrations (0, 6.4 μM, 32 μM, 160 μM, 800 μM, 4 mM, 20 mM) of Cu^{2+}. (b) Comparison of the MB absorption at 664 nm in the

mixed solution of 10 mM H_2O_2 and different concentrations (0, 6.4 μM, 32 μM, 160 μM, 800 μM, 4 mM, 20 mM) of Cu^{2+}. The •OH yield relies little on the Cu^{2+} concentration, indicating the catalyst role of Cu^{2+} in the Fenton-like reaction for converting H_2O_2 into •OH.

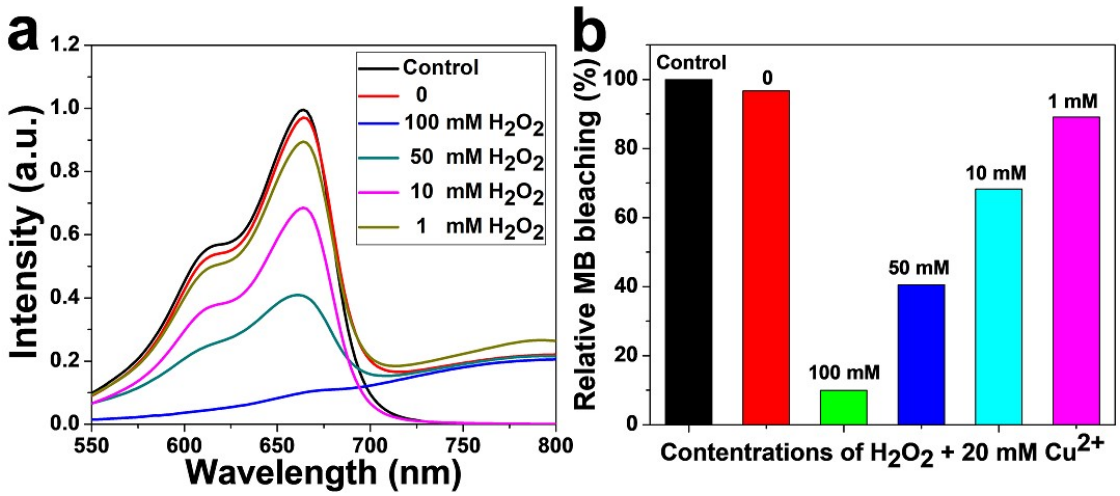

Figure S15. Evaluation of •OH yield (determined by the decay of MB absorption at λ = 664 nm) arising from the Fenton-like reaction between 20 mM Cu^{2+} and varied concentrations of H_2O_2. (a) UV/Vis absorption spectra of MB in the mixed solution of 20 mM Cu^{2+} and different concentrations (0, 1 mM, 10 mM, 50 mM, 100 mM) of H_2O_2. (b) Comparison of the MB absorption at 664 nm in the mixed solution of 20 mM Cu^{2+} and different concentrations (0, 1 mM, 10 mM, 50 mM, 100 mM) of H_2O_2. The •OH yield depends on the H_2O_2 concentration.

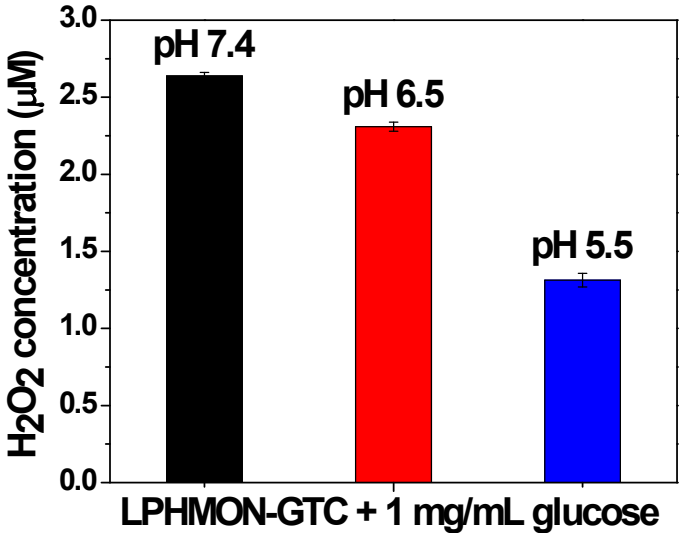

Figure S16. The generated H_2O_2 concentrations after 1 h reaction between LPHMON-GTC and glucose (1 mg/mL) in PBS solutions (initial pH 7.4, 6.5, 5.5). The generated H_2O_2 concentration was decreased with the lowering pH, which might be attributed to the lower pH-induced release of more Cu^{2+} to accelerate the Fenton-like reaction by catalyzing the conversion of more H_2O_2 into •OH.

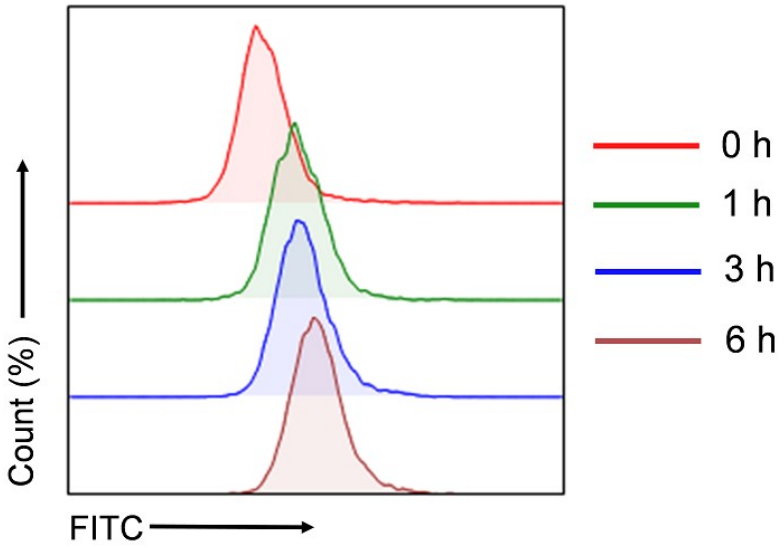

Figure S17. Flow cytometry analysis of cell uptake of FITC-labeled LPHMON after incubation with Hepa1-6 cells for 0, 1, 3, and 6 h.

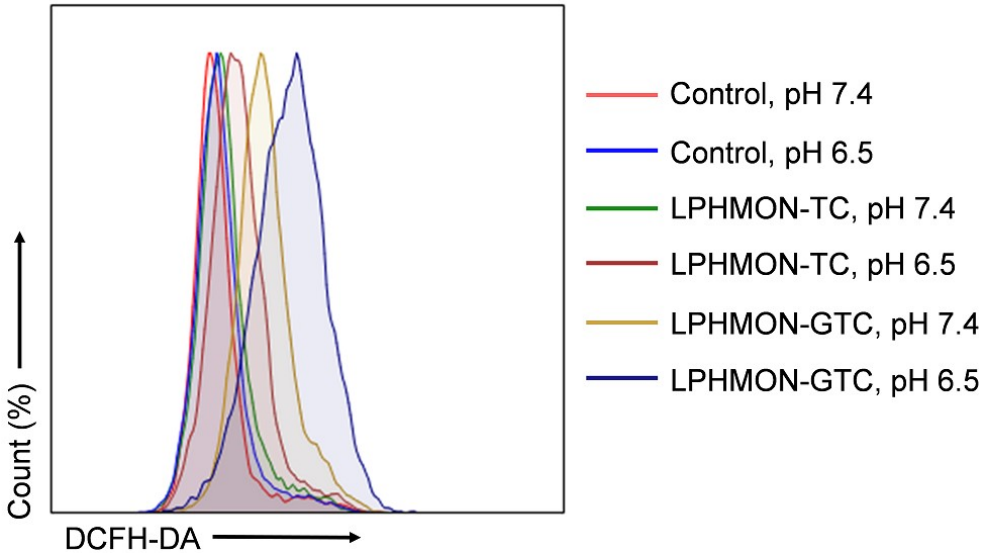

Figure S18. Flow cytometry analysis of intracellular ROS generation (using an ROS indicator, DCFH-DA) in Hepa1-6 cells after 6 h of incubation with PBS (control), LPHMON-TC, and LPHMON-GTC at pH 7.4 and 6.5, respectively.

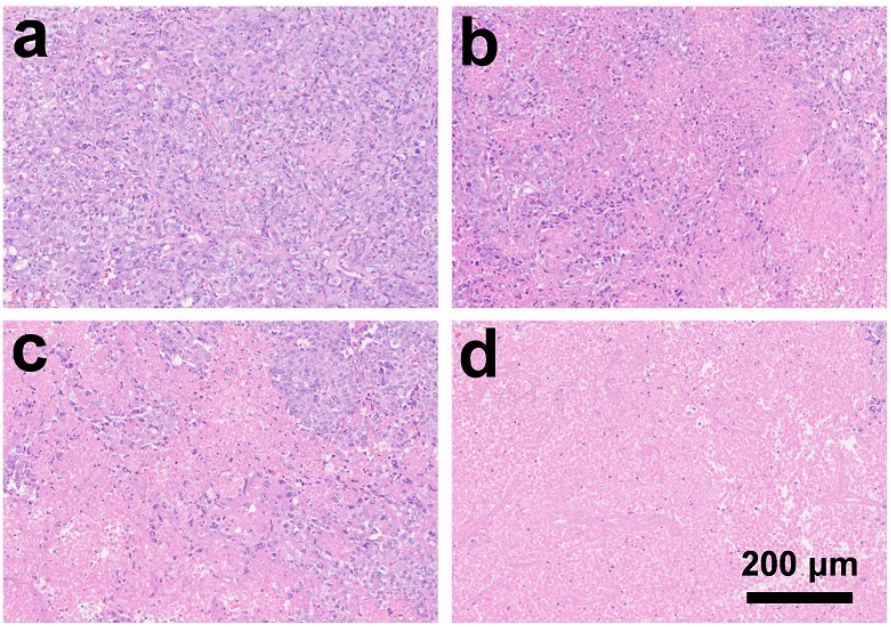

Figure S19. H&E-stained tumor sections from Hepa1-6 tumor-bearing mice after treated with (a) PBS, (b) LPHMON-TC, (c) LPHMON-G, and (d) LPHMON-GTC. The degree of tumor cell apoptosis/necrosis reflects the therapeutic effect of the corresponding treatment. Scale bar: 200 μm.

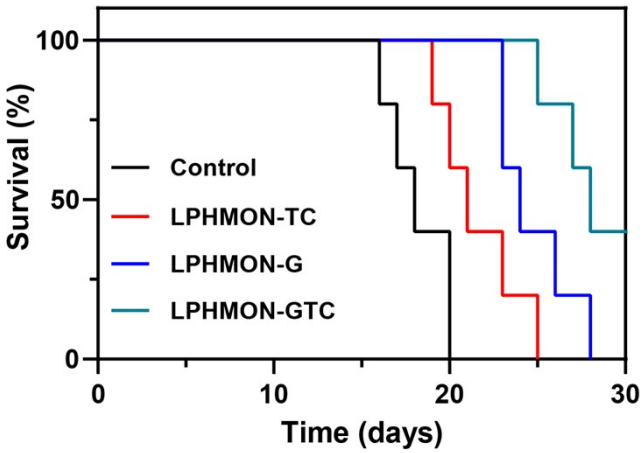

Figure S20. Survival curves of Hepa1-6 tumor-bearing mice after different treatments.

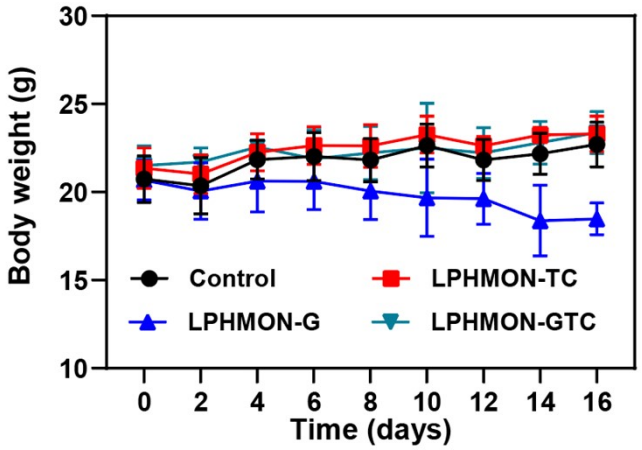

Figure S21. Body weight change curves of Hepa1-6 tumor-bearing mice after different treatments. n = 5, mean ± s.d.

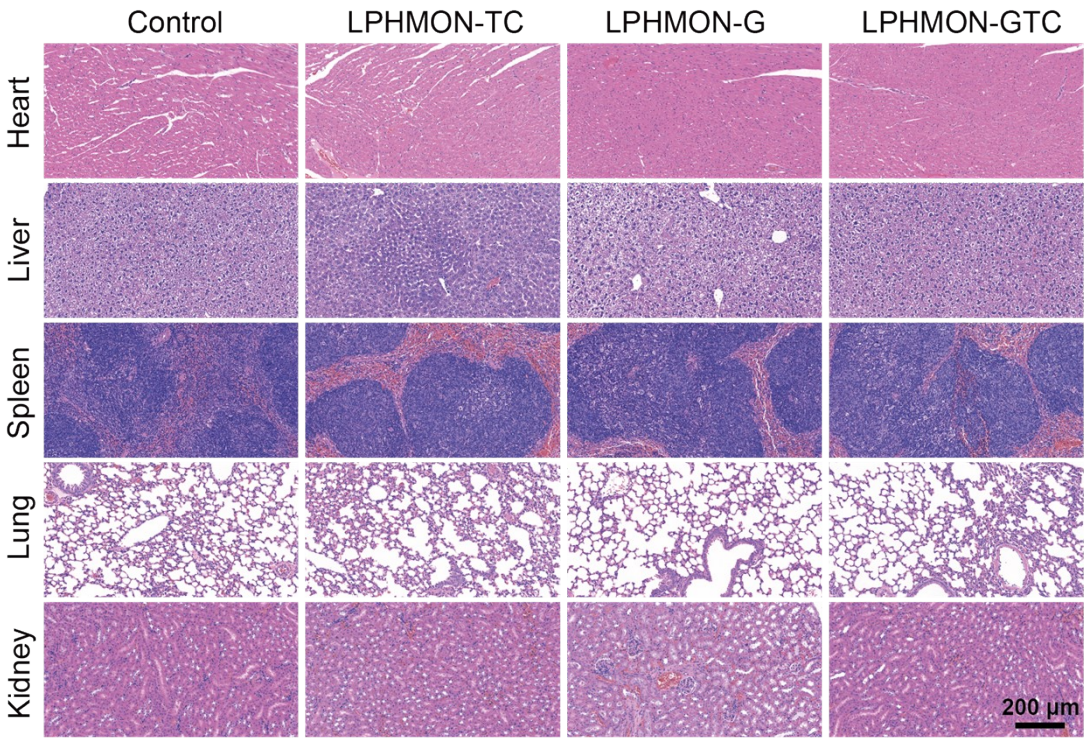

Figure S22. Representative H&E staining of major organs from Hepa1-6 tumor-bearing mice after different treatments. Scale bar, 200 μm.